DESIGN AND OPTIMIZATION OF A DOUBLE-INTAKE AND ROTOR SQUIRREL CAGE FAN USING OPENFOAM AND METAMODELS

Alla Eddine BENCHIKH LE HOCINE, Sébastien PONCET,
Hachimi FELLOUAH

Department of Mechanical Engineering, Université de Sherbrooke,
2500 Boulevard de l'Université, Sherbrooke (QC), J1K 2R1, Canada

SUMMARY

In the present study, a powerful double-intake and rotor squirrel cage fan is designed and optimized by using a developed optimization process loop based only on open source libraries: Dakota, Salome and OpenFoam. Thirteen design parameters are selected for the trimming and in the impellers, blades and volute regions. The total efficiency and the force applied on the impeller are improved by maximizing and minimizing their values, respectively. A coupling was achieved between CFD, Latin Hypercube Sampling, Kriging metamodel and the Efficient Global Optimization to find the optimal design. The design for Configuration 3 improved the initial efficiency by 7.9 % and was validated successfully against experiments with an error of 1.1 %.

INTRODUCTION

Range hoods are widely used during cooking activities due to their ability to extract emitted particles, which cause the decrease of the air quality level and may induce respiratory diseases. Many researches have been done in order to improve the captation of range hoods while decreasing the generated noise. Most of the range hoods are equipped with a squirrel cage fan (SCF). The SCF has been extensively used for decades in HVAC systems and other household appliances (bath room) [1]. The SCF is a special centrifugal fan, also known as forward-curved multi-blade centrifugal fan. The disadvantages of the SCF are: (I) the complex flow mechanisms in the rotor region, especially around the blades where the flow is separated due to their two-dimensional circular arc profile [2]; (II) low generated flowrate and pressure drop between the inlet and the outlet. The double-intake SCF has the ability to fill in the low capacity of the SCF by increasing the pressure drop and the flowrate. However, the complex flow mechanisms are subject to an optimization process in order to improve its efficiency.

Design of experiments (DOE) and metamodels have been used in the optimization process of the SCF due to their ability to understand the influence of the different design parameters and converge toward

an optimal design. Zhou et *al*. [3]. Zhou et *al*. [3] used for the design of an arc blade a modified Hicks-Henne function, where the three amplitude coefficients were selected as input parameters. The authors focused only on the blade profile function while the other parts of the SCF remained identical. For the CFD, the commercial software ANSYS was used with a 3D incompressible solver and the k-ω SST turbulence closure. The sampling points were obtained by a latin hypercube design and the optimal design was selected by the NSGA-II method. The Kriging metamodel construction was accomplished with the commercial software Matlab. The authors found that the values obtained by the Kriging model were accurate with average relative errors of 2.7 % and 2.6 % for the efficiency and flow rate, respectively. The selected optimal design improved the efficiency by 4.2 % compared to the initial one. The numerical results were validated against experimental data with a maximum error of 3.2 % in terms of efficiency. Kim and Seo [4] studied numerically the influence of cutoff location and radius, and impeller width on the SCF efficiency. For the optimization process, the authors employed the quadratic polynomial response surface method and CFD. The 3D incompressible solver incorporated the standard k-ε model available in the commercial software CFX. The commercial software SPSS was used for the construction of the metamodel. The validation of the numerical results was accomplished against the experimental data of Kim and Kang [5] obtained by a hot-wire probe around the initial SCF design. A maximum error of 20 % was observed between the numerical and experimental radial velocity at the inlet. Kim and Seo [4] found that the quadratic polynomial model improved the maximum efficiency and the static pressure coefficient by 38.8 % and 1.7 %, respectively. However, any validation of the obtained results was accomplished either by CFD or experiments.

Most of the published studies so far focused on the investigation and the optimization of the single intake SCF. Yet, they used commercial softwares for the CFD calculations and optimization processes [1, 6, 7]. In the actual study, a double-intake and rotor SCF is designed and optimized by coupling 3D simulations and metamodels in order to improve the efficiency and the applied force on the impeller. All the process is accomplished through open-source softwares. 11 design parameters are selected in the rotor and volute regions as inputs for the optimization process. For the blade trimming, two design parameters are employed. The sampling is accomplished with the Latin Hypercube Sampling (LHS) approach and the CFD results are used to construct a response surface of a Surrogate Based Optimization (herein Kriging). In order to expand the Kriging model predictions, the Efficient Global Optimization (EGO) is employed to obtain the best configuration. The optimal configuration is finally carefully validated against experimental data.

NUMERICAL MODELING

A 3D steady-state Navier-Stokes incompressible flow solver has been employed by using the open source OpenFOAM 6 libraries to model the flow inside the double-intake SCF.

Geometrical modeling

Figure 1 displays multiple views of the double-intake SCF in Configuration 1. For all configurations, a Latin Hypercube Sampling (LHS) has been used for sampling in the Design of Experiments (DoE) method. The main difference between the three configurations is the number of the selected design parameters. In configuration 1, 2 and 3 eleven, six and two designparameters are selected, respectively. The hub in the three configurations has a conical shape and is constructed with a quadratic Bezier curve. The hub's diameter and height are 0.1042 m and 0.0298 m, respectively. The motor housing is placed in the second wheel region and has a cylindrical shape with a diameter and height of 0.0838 m and 0.1016 m, respectively. The first wheel contains the hub. The double-intake SCF is a 60 bladed rotor. The blades are equipped with 4 digit NACA (0012).

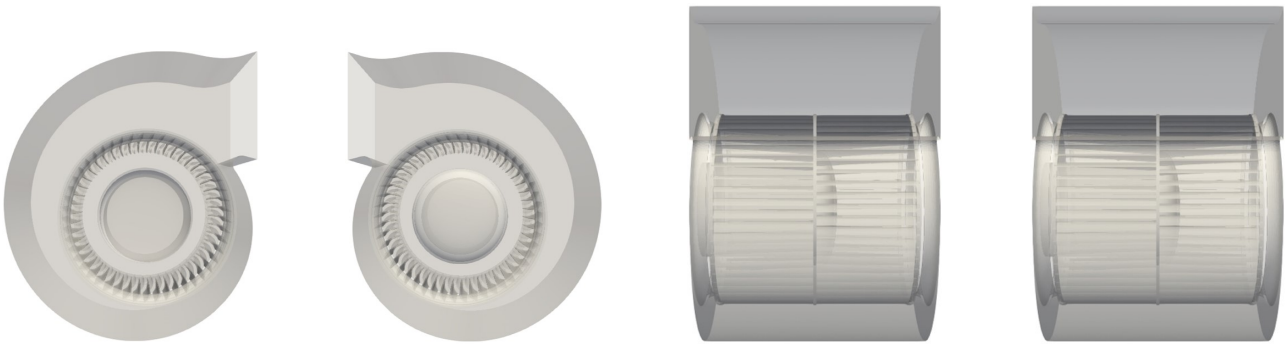

(a) left *(b) right* *(c) front* *(d) rear*

Figure 1: Different views of the double-intake SCF.

The SCF is placed in an open environment represented herein by a sphere having a diameter of $D_{ext} = 1.3\ m$ (Fig.2). The volute is connected to an exit duct with a length of $L_p = 0.61\ m$. The diameter of the exit duct was expanded with an angle of 7° in order to enhance the calculation stability and to reduce the head losses.

Numerical methods

The 3D steady state incompressible Reynolds averaged Navier-Stokes (RANS) solver named SimpleFoam is used to model the flow dynamics around the double-intake SCF. The SimpleFoam has already shown its ability to model accurately the flow inside the rotating impeller with the multiple reference frame (MRF) approach [8, 9, 10]. Furthermore, this solver offers time saving, especially in an optimization process where more than 400 calculations are performed simultaneously.

A fully second-order scheme is used for the spatial discretization in order to minimize excessive numerical dissipation. The Laplacian and gradient terms are discretized by using a bounded Gauss linear numerical scheme. A linear approach is selected for the interpolation scheme. The SIMPLE (Semi-Implicit-Method for Pressure-Linked Equations) algorithm [11] enables to overcome the pressure-velocity coupling. The generalized geometric-algebraic multi-grid (GAMG) solver with the combined Diagonal incomplete-Cholesky/Gauss Seidel (symmetric) smoother is selected to solve the pressure. The preconditioned bi-conjugate gradient (PBiCG) solver with Diagonal incomplete-LU (DILU) pre-conditioner is used to solve the rest of the discretized equations.

The turbulent flow is modeled by the two-equation eddy viscosity Shear Stress Transport $k-\omega$ model ($k-\omega$ SST) developed by Menter [12]. The $k-\omega$ SST model combines the robust formulation of the $k-\omega$ Wilcox model [13] in the near wall region and the $k-\varepsilon$ away from the wall. Very satisfactory results were obtained by multiple authors when using the $k-\omega$ SST turbulence closure for modeling turbulent flows in different fan configurations [14, 15, 16].

The boundary conditions of the computational domain are shown in Figure 2. Three regions are distinguable: the rotor (impeller), the surrounding environment and the volute with the exit pipe. The rotor region includes the two impellers, fan blades, the rotating ring and the hub. The two rotors are connected through the bottom plate and rotate at 1844 rpm. A Python script was developed to recalculate and adjust the value of the rotating speed for each configuration in order to converge toward the target total pressure. An inlet mass flowrate condition of 0.3258 kg/s (590 cfm) is imposed at the sphere surface with a turbulence intensity of 5 %. The air properties are assumed to be constant and are evaluated at an ambient temperature of 293 K. A no slip wall condition is imposed at the blade surfaces, hub, rotating ring and the disc plate. The same condition is also applied on the volute and the exit pipe surfaces. A pressure outlet condition is imposed at the pipe outlet surface where a static pressure of 216.781 Pa (0.87 inch water) is fixed. The multiple reference frame (MRF) approach is

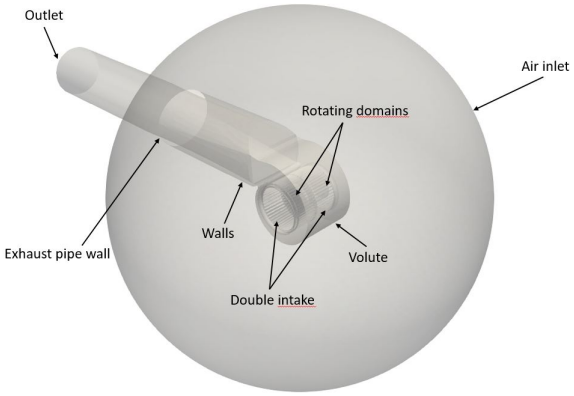

Figure 2: 3D sketch of the computational domain.

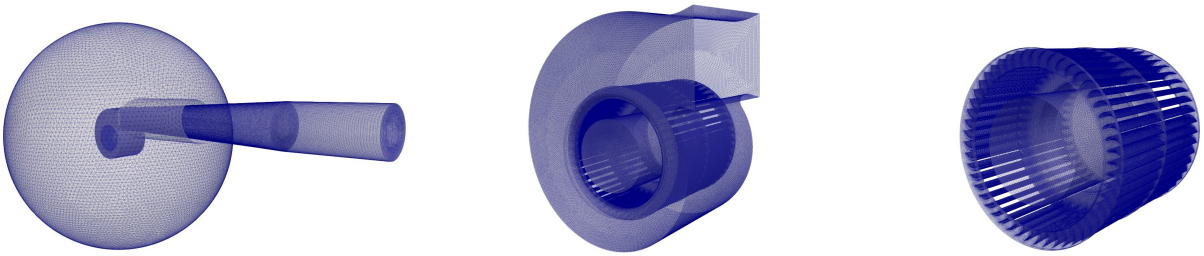

(a) whole domain *(b) volute* *(c) rotor*

Figure 3: Different views of the mesh distribution.

used to model the rotating motion of the rotor region.

Figure 3 shows different views of the unstructured fine grid mesh generated by the open-source software Salome. The mesh is composed of tetrahedral and prismatic elements. Multiple mesh refinements with factors equal to 4 and 3 are imposed in the volute and the exit pipe, respectively. Ten prismatic layers are generated around the blades with a stretching factor of 1.1. The average total number of elements is around 37.8 million cells, with 20.1 and 9.2 million cell elements in the rotor and volute regions, respectively. The maximum value of the wall coordinate (y^+) is lower than 0.9, which satisfies the low-Reynolds number approach.

The calculations were run using HPC facilities provided by Calcul Québec. Each RANS calculation took from 3 to 4 days using 32 processors (AMD Opteron 6172). During all the optimization process, around 12800 processors were used. The convergence is achieved when the global fan efficiency deviation is below 0.1 % and all residuals are lower than 10^{-7}.

OPTIMIZATION PROCESS AND METHODS

Optimization loop

Figure 4 displays the optimization procedure. Firstly, the design space is determined by the input parameters' minimum and maximum bounds. In Configuration 1, eleven input parameters are selected, while in Configuration 2, only the relevant design parameters are kept (Tab.2). In Configuration 3, the optimal design is trimmed using two design parameters. The input variables are:

1. D_1/D_2 is the ratio between the wheel interior and external diameters;
2. β_1 is the blade leading edge angle (angle of attack);
3. β_2 is the blade trailing edge angle (outlet angle);

4. R_c/D_2 is the ratio between the cutoff radial position and the wheel external diameter;
5. θ_c is the cut-off angular position;
6. θ_f is the final radial angular position of the external spiral (volute);
7. IV/D_2 is the ratio between the internal housing inlet height and the external wheel diameter;
8. P is the ratio between the position of the maximum camber and blade's chord length ;
9. H_2 is the height of one impeller;
10. D_2 is the wheel external diameter;
11. r_c/D_2 is the ratio between the cutoff radius and the wheel external diameter;
12. Z_1 is the position of the trimming along the blade;
13. D_c/D_2 is the ratio between the cutting diameter and the external diameter of the wheel.

Table 1: Design parameters with lower and upper bounds.

Design parameters	lower bound	upper bound
D_1/D_2 [-]	0.8	0.9
β_1 [°]	85	115
β_2 [°]	28	45
R_c/D_2 [-]	0.560	0.625
θ_c [°]	-30	-10
θ_f [°]	270	290
IV/D_2 [-]	0.05	0.1
D_2 [m]	0.1524	0.1778
r_c/D_2 [-]	0.035	0.07
P [-]	0.3	0.5
h_{max} [m]	0.08255	0.09652
Z_1 [m]	0.001524	0.055702
D_c/D_2 [-]	0.2	0.6

The different input variables are introduced to Dakota and a design of experiment (DOE) is conducted by using the Latin hypercube sampling (LHS). The LHS is a stratified sampling method where the uncertain variable range is divided into N requested samples. A random sample is selected from each of the segments. The N values are combined in a shuffling operation to construct a set of N parameter vectors with a correlation structure.

In the next step, Salome is loaded and the entire geometry and the computational domain are created automatically. A Python script is used to check any irregularity in the geometry as holes, bad intersections, etc. After, the Salome mesh library is executed according to a pre-set Python script with

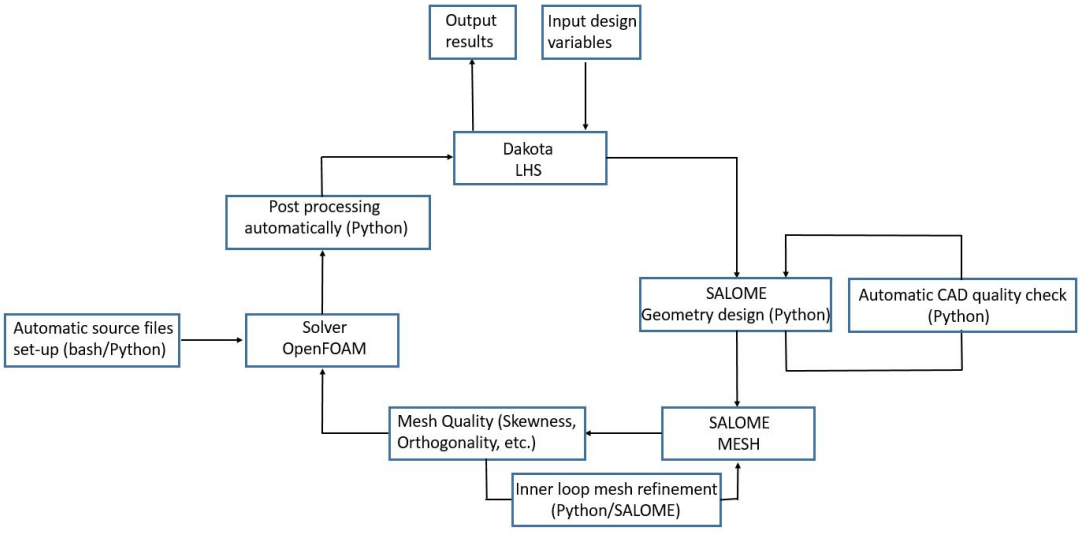

Figure 4: Chart of the optimization loop process.

all the mesh parameters. A CheckMesh function of OpenFOAM is used in order to ensure the mesh quality. Then, the OpenFOAM directories are created automatically and all the calculations are run simultaneously. Once the calculations finish, the objective functions, namely the global efficiency and the force applied on the impellers, are calculated and saved in a results file.

Metamodel approach

The metamodel construction process is displayed in Fig.5. Multiple surrogate models exist and have been tested in the past such as radial basis functions, polynomial regression, neural networks, etc. In this study, the Kriging metamodel is selected due to its ability to predict accurately the efficiency [17]. It is based on a Gaussian stochastic process of the modeled objective functions. Mathematically, the Kriging function prediction at a point (design parameter) x is defined as:

$$\hat{f}(x) = \hat{\mu} + \psi R^{-1}(Y - 1\hat{\mu}) \tag{1}$$

where $\hat{\mu}$ is the maximum likelihood estimator and $\hat{f}(x)$ is the predicted objective function. Y represents a set with a dimension N of the calculated data and is expressed as follows:

$$Y = [f(x^{(i)}) \ldots f(x^{(N)})] \tag{2}$$

Herein, $f(x)$ represents the value obtained by CFD. ψ are the basis functions.

In addition to the Kriging metamodel, the efficient global optimization (EGO) method is applied to predict the objective functions. The EGO has been developed by Jones et *al*. [18] and is based on the Kriging metamodel. However, the EGO has the ability to select the next sample point with the maximum probability to converge toward the optimal values. The probability is defined as an expected improvement (EI) function calculated as:

$$E(I(x)) = \left(f_{min} - \hat{f}\right) \Phi\left(\frac{f_{min} - \hat{f}}{s}\right) + s\phi\left(\frac{f_{min} - \hat{f}}{s}\right) \tag{3}$$

where f_{min} is the obtained minimum value from the CFD calculations and $\hat{f}$ is the value predicted by the Kriging model. s is the standard error. $\phi(.)$ and $\Phi(\Delta)$ are the standard normal density and distribution function, respectively. $I(x)$ is the improvement at the point x. The EGO is an iterative process and will continue until a global optimal is found and validated.

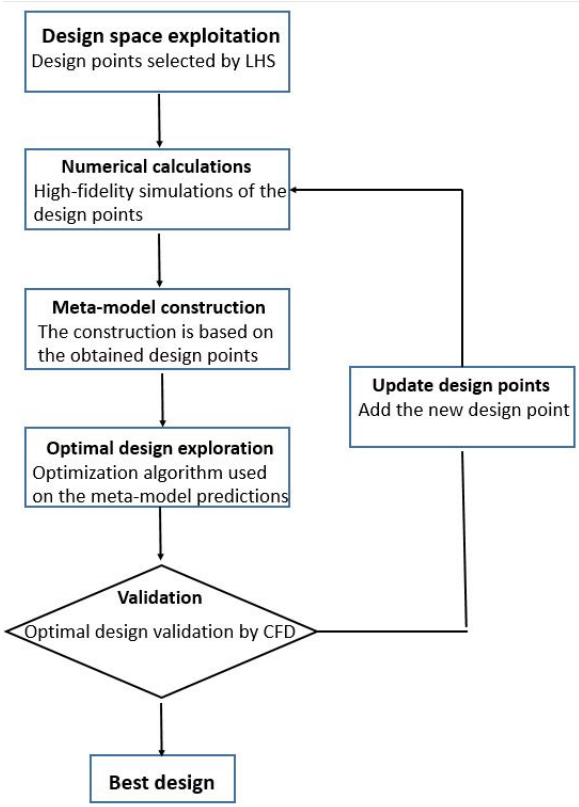

Figure 5: Chart of the metamodel optimization process.

RESULTS

In this section, the results of the optimization process are presented for the three configurations.

Performance comparison

The optimal values of the total fan efficiency ε and the force applied on the impellers F_{xy} are determined after completing all the optimization process for the LHS approach and constructing the surrogate models. The objective of the optimization is to minimize F_{xy} in order to reduce the mechanical damage on the impellers while maximizing ε.

The predicted values of the objective functions obtained by the different approaches are presented in Table 2. In all configurations, the Kriging model predicts with accuracy the ε and F_{xy} values with a maximum error of 3 % and 4.5 %, respectively. The main limitation of the Kriging response values is the existence of a highly turbulent flow with 3D vortices interacting with the impeller blades. In Configuration 1, The Kriging model improves the efficiency by 0.1 % compared to the optimal LHS design. The EGO converges toward an optimal design after 5 iterations and enhances ε while decreasing F_{xy} by 2.6 % and 30.7 %, respectively. The EGO approach expands the design space compared to the Kriging model, which increases the probability to find an optimal design that meets the requirements. In Configuration 2, only the relevant parameters are selected and the total design parameters are reduced to 6, which will decrease the data noise and allows a remarkable improvement by 5.2 % and 29.7 % of the efficiency and applied force, respectively, compared to Configuration 1's LHS design. As in Configuration 1, the optimal design with the EGO model improves the results, specifically F_{xy} by 20.6 % compared to the Kriging model validation. In Configuration 3, the optimal design of configuration 2 (EGO) is trimmed according to the design parameters Z_1 and D_c/D_2. The LHS results show a slight improvement in the efficiency by 0.1 %. However, F_{xy} is impaired by 1.1 %.

Table 2: Summary of the predicted objective function values by the different models. Relative errors (%) compared to the OpenFOAM validation are indicated between (−). The design parameters with / are not considered.

Configurations	Method	D_2 [m]	D_1/D_2 [-]	P [-]	β_1 [°]	β_2 [°]	R_c/D_2 [-]	r_c/D_2 [-]	θ_c [°]	θ_f [°]	IV/D_2 [-]	h_{max} [m]	Z_1 [m]	D_r/D_2 [-]	ε [%]	F_{xy} [N]
Configuration 1	LHS	0.1745	0.87768	0.4713	86.869	29.336	0.56405	0.04426	-28.8634	277.776	0.06001	0.0924	/	/	52.2	2.94006
	Kriging	0.1666	0.8056	0.4999	107.4029	38.1654	0.5673	0.0509	-28.6150	288.2595	0.06887	0.0852	/	/	53.5(1.2 %)	2.6001 (4.1 %)
	OF validation	0.1666	0.8056	0.4999	107.4029	38.1654	0.5673	0.0509	-28.6150	288.2595	0.06887	0.0852	/	/	52.3	2.7116
	EGO	0.1524	0.8358	0.4593	109.6642	28.8128	0.5977	0.0695	-27.1734	289.7339	0.0587	0.0837	/	/	54.8	2.0362
Configuration 2	LHS	0.1658	0.8132	/	/	36.11	0.5727	/	/	-13.6	/	0.0892	/	/	57.4	2.064
	Kriging	0.1662	0.8396	/	/	36.4	0.5935	/	/	-27.61	/	0.0929	/	/	61.9 (2.9 %)	2.355 (4.5 %)
	OF validation	0.1662	0.8396	/	/	36.4	0.5935	/	/	-27.61	/	0.0929	/	/	59	2.466
	EGO	0.1676	0.8088	/	/	37.6	0.5709	/	/	-29.19	/	0.0971	/	/	59.8	1.959
Configuration 3	LHS	0.1676	0.8088	/	/	37.6	0.5709	/	/	-29.19	/	0.0971	2.19	0.60	56.9	1.98
	Kriging	0.1676	0.8088	/	/	37.6	0.5709	/	/	-29.19	/	0.0971	1.13	0.62	59.6 (3 %)	2.19 (3.1 %)
	OF validation	0.1676	0.8088	/	/	37.6	0.5709	/	/	-29.19	/	0.0971	1.13	0.62	56.9	2.26
	EGO	0.1676	0.8088	/	/	37.6	0.5709	/	/	-29.19	/	0.0971	1.13	0.40	60	2.11

As observed in Configurations 2 and 3, the EGO model provides the optimal design with ε and F_{xy} of 60 % and 2.1 N, respectively.

Mean flow field

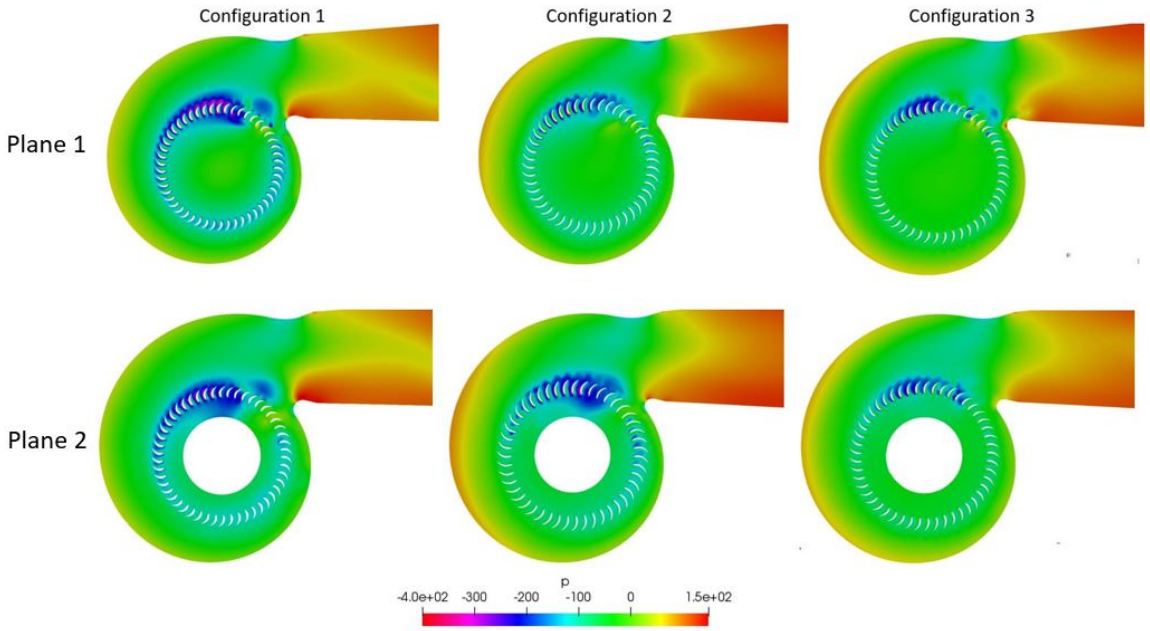

Figure 6: Distribution of the static pressure p (Pa) on planes 1 and 2 for optimal configurations 1, 2 and 3.

Figure 6 displays the 2D contours of the pressure distribution on planes 1 and 2. They are located at the mid-height of the impellers 1 and 2, respectively. The hole in plane 2 represents the shape of the motor housing. In Configuration 1, the flow in both impellers is comparable with an acceleration near the top left of the impeller and a recirculation region around the cut-off. However, in Configurations 2 and 3, the recirculation disappears and the acceleration region is smaller and concentrated in the top region near the 0° angular position. The acceleration region in the three configurations collapses with the blade separation (seen from the total pressure not shown here), which confirms the obtained results in Table 2. As the flow around the blade is attached, the total efficiency is increased. The motor housing has any effect on the pipe flow patterns. However, in the rotor region, the housing causes an obstruction leading to higher flow acceleration as the flow rate is constant.

Validation

An experimental prototype was built based on the design of configuration 3 which produced the optimal objective functions. The static pressure and voluminal flowrate were recorded experimentally and compared to the numerical results. Experimentally, the computational domain was reproduced in

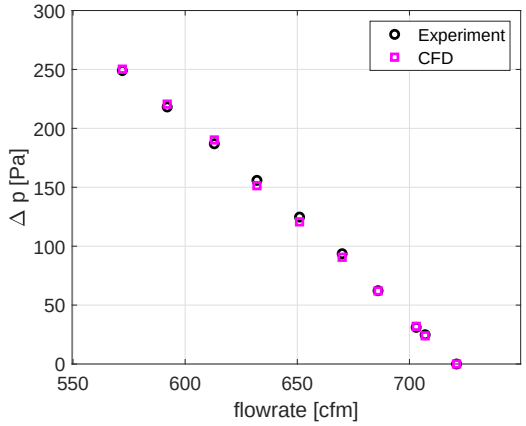

Figure 7: Pressure drop Δp of the fan as a function of the flowrate. Comparison between the present solver (dashed lines) and experiments (circles).

order to avoid any discrepancies (Fig.2). The experimental process consists of recording the generated flowrate by fixing the rotation speed of the fan and the outlet pressure. The effective surface at the exit was controlled to vary the outlet pressure. The velocity and the pressure were measured by a digital manometer with an accuracy of ± 1 % and ± 3 %, respectively. The CFD calculation predicts very accurately the pressure drop for all flowrates with a maximum error of 3.6 % at 670 cfm. At the design point (590 cfm), the pressure drop is predicted with an error of 1.1 %.

CONCLUSION

This paper reported numerical results of the double-intake SCF optimization, using open source libraries. An optimization loop was developed using Dakota, Salome and OpenFOAM. The LHS and metamodels were used to deliver the optimal design with the best objective functions values. Multiple configurations have been tested with different design parameters and trimming processes.

Configuration 3 produced the optimal values of the objective functions, by offering a trade off between the efficiency ε and the force applied on the impeller F_{xy}. By removing the nonsignificant parameters in Configuration 1 and by applying a trimming on the blades, ε and F_{xy} were improved by 7.9 % and 28.2 %, respectively. For all configurations, the EGO approach converged toward the optimal design due to the expansion of the design space and the improvement prediction.

The distributions of the static pressure p in planes 1 and 2 showed a flow acceleration in the impeller top region. In the impeller with the motor housing, the flow is more accelerated due to the obstruction. In Configuration 1, a recirculation region was observed near the cut-off region in both impellers. In Configurations 2 and 3, the acceleration region is more concentrated near the 0° angular position.

Future works should integrate the blade sweeping effect along the span. Furthermore, running unsteady calculations based on more advanced turbulence closures are deemed necessary to investigate the flow dynamics of the coherent structures near the cut-off region.

ACKNOWLEDGMENT

All calculations have been done using the computational resources of the Compute Canada network, which is here gratefully acknowledged.

REFERENCES

[1] K. Wang, Y. Ju, and C. Zhang, "Experimental and numerical investigations on effect of blade trimming on aerodynamic performance of squirrel cage fan," *International Journal of Mechanical Sciences*, vol. 177, no. 105579, **2020**.

[2] F. P. Bleier, *Fan Handbook: Selection, Application, and Design*.

[3] S. Zhou, H. Zhou, K. Yang, H. Dong, and Z. Gao, "Research on blade design method of multi-blade centrifugal fan for building efficient ventilation based on Hicks-Henne function," *Sustainable Energy Technologies and Assessments*, vol. 43, no. 100971, **2021**.

[4] S.-J. Seo and K.-Y. Kim, "Design optimization of forward-curved blades centrifugal fan with response surface method," ser. Proceedings of the ASME Heat Transfer/Fluids Engineering Summer Conference, vol. 2 A, Charlotte, North Carolina, USA, 01 **2004**, pp. 551–556.

[5] J. K. Kim and S. H. Kang, "Effects of the scroll on the flow field of a sirocco fan," ser. Proceedings of the ISROMAC-7, Hawai, USA, **1997**, pp. 1318–1327.

[6] S.-C. Lin and M.-L. Tsai, "An integrated performance analysis for a backward-inclined centrifugal fan," *Computers and Fluids*, vol. 56, pp. 24 – 38, **2012**.

[7] M. Gholamian, G. K. M. Rao, and B. Panitapu, "Effect of axial gap between inlet nozzle and impeller on efficiency and flow pattern in centrifugal fans, numerical and experimental analysis," *Case Studies in Thermal Engineering*, vol. 1, no. 1, pp. 26 – 37, **2013**.

[8] G. Angelini, T. Bonanni, A. Corsini, G. Delibra, L. Tieghi, and D. Volponi, "Optimization of an axial fan for air cooled condensers," *Energy Procedia*, vol. 126, pp. 754–761, **2017**.

[9] V. D'Alessandro, S. Montelpare, R. Ricci, and A. Zoppi, "Numerical modeling of the flow over wind turbine airfoils by means of Spalart -Allmaras local correlation based transition model," *Energy*, vol. 130, pp. 402–419, **2017**.

[10] F. Bothe, C. Friebe, M. Heinrich, and R. Schwarze, "CFD Simulation of Incompressible Turbomachinery —A Comparison of Results From ANSYS Fluent and OpenFOAM," ser. Proceedings of ASME Turbo Expo: Power for Land, Sea, and Air, vol. 2B: Turbomachinery, Düsseldorf, Germany, **2014**.

[11] S. V. Patankar and D. B. Spalding, "A calculation procedure for heat, mass and momentum transfer in three-dimensional parabolic flows," *International Journal of Heat and Mass Transfer*, vol. 15, no. 10, pp. 1787–1806, **1972**.

[12] F. R. Menter, "Two-equation eddy-viscosity turbulence models for engineering applications," *AIAA Journal*, vol. 32, no. 8, pp. 1598–1605, **1994**.

[13] D. C. Wilcox, "Reassessment of the scale-determining equation for advanced turbulence models," *AIAA Journal*, vol. 26, no. 11, pp. 1299–1310, **1988**.

[14] L. Daróczy, G. Janiga, K. Petrasch, M. Webner, and D. Thévenin, "Comparative analysis of turbulence models for the aerodynamic simulation of h-Darrieus rotors," *Energy*, vol. 90, pp. 680 – 690, **2015**.

[15] M. Carnevale, F. Wang, and L. Di-Mare, "Calculation of Intake-Fan-Bypass Interaction With a Fan Similarity Model," ser. Proceedings of ASME Turbo Expo: Power for Land, Sea, and Air, vol. 2C: Turbomachinery, Oslo, Norway, **2018**.

[16] A. Theis, T. Reviol, and M. Böhle, "Analysis of the Losses in an Axial Fan With Small Blade Aspect Ratios Using CFD-Technique and Laser Doppler Anemometry," ser. Proceedings of ASME Turbo Expo: Power for Land, Sea, and Air, vol. 2A: Turbomachinery, Virtual conference, **2020**.

[17] X. Wu, B. Liu, N. Ricks, and G. Ghorbaniasl, "Surrogate models for performance prediction of axial compressors using through-flow approach," *Energies*, vol. 13, no. 1, p. 169, **2019**.

[18] D. Jones, M. Schonlau, and W. Welch, "Efficient global optimization of expensive black-box functions," *Journal of Global Optimization*, vol. 13, pp. 455–492, **1998**.